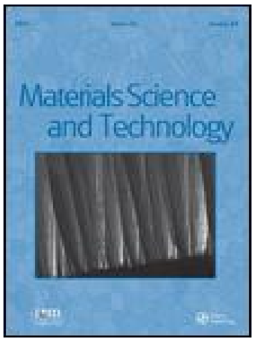

Materials Science and Technology

ISSN: 0267-0836 (Print) 1743-2847 (Online) Journal homepage: http://www.tandfonline.com/loi/ymst20

A cellular automaton-finite difference simulation of the ausferritic transformation in ductile iron

A. D. Boccardo, P. M. Dardati & L. A. Godoy

To cite this article: A. D. Boccardo, P. M. Dardati & L. A. Godoy (2018): A cellular automaton-finite difference simulation of the ausferritic transformation in ductile iron, Materials Science and Technology, DOI: 10.1080/02670836.2018.1475035

To link to this article: https://doi.org/10.1080/02670836.2018.1475035

MATERIALS SCIENCE AND TECHNOLOGY
https://doi.org/10.1080/02670836.2018.1475035

A cellular automaton-finite difference simulation of the ausferritic transformation in ductile iron

A. D. Boccardo[a,b], P. M. Dardati[b] and L. A. Godoy[a,c]

[a]Instituto de Estudios Avanzados en Ingeniería y Tecnología, IDIT, CONICET-Universidad Nacional de Córdoba, Córdoba, Argentina; [b]Grupo de Investigación y Desarrollo en Mecánica Aplicada, GIDMA, Facultad Regional Córdoba, Universidad Tecnológica Nacional, Córdoba, Argentina; [c]Facultad de Ciencias Exactas, Físicas y Naturales, Universidad Nacional de Córdoba, Córdoba, Argentina

ABSTRACT
The development of the ausferritic transformation of a ductile iron was analysed using a novel cellular automaton-finite difference model, which considers geometrical details of the microstructure, nucleation of the new phase at graphite nodule surface, contact between growing phases, and carbon diffusion in austenite. The role of nucleation, austenite carbon enrichment, and contact between phases in the different stages of the growth kinetics was studied. Moreover, a parametric study was performed to investigate the influences of graphite nodule size, and austenitizing and austempering temperatures on the required time to end the transformation and final phase fractions. The obtained results are in agreement with experimental data reported in the literature.

ARTICLE HISTORY
Received 3 February 2018
Accepted 7 May 2018

KEYWORDS
Ausferritic transformation; ductile iron; cellular automaton-finite difference analysis

1. Introduction

Austempered ductile iron (ADI) is an alloy of Fe–C–Si, which is employed in several applications due to its wide range of mechanical properties and low manufacturing cost. The microstructure of ADI is formed by graphite nodules inserted in an ausferritic matrix, as is shown in Figure 1. At ambient temperature, this matrix is formed by sheaves and austenite blocks. A sheaf is a wedge-shaped micro-constituent that is formed by ferrite platelets (subunits) and austenite films [1,2].

The complex microstructure of ADI is formed during the ausferritic transformation that takes place at the austempering temperature (523 K (250°C) $\leq T_A \leq$ 723 K (450°C)). The austenite transforms into ferrite subunits by means of the displacive growth mechanism that involves a continuous process of: (a) nucleation, (b) growth without carbon diffusion, and (c) carbon rejection from carbon-supersaturated ferrite to austenite [1,3].

In the literature review, only a few models were found about the kinetics of the ausferritic transformation in ductile iron. Thomson et al. [3] presented a modified steel model considering a displacive growth mechanism. Ferrite subunits nucleate continuously within austenite that has a homogeneous carbon concentration. The nucleation law considers the austempering temperature, austenite carbon concentration, and the number of subunits that have already nucleated. Kapturkiewicz et al. [4] presented a model in which the thickness of ferrite lamellae of infinite length grows by means of carbon diffusion (diffusive mechanism growth). A continuous nucleation of lamellae is considered following Avrami's equation. Hepp et al. [5] proposed a model in which the thicknesses of acicular ferrites grow by means of carbon diffusion. The ferrite particles are oriented parallel to each other, whose separation is determined by the number of subunits nucleated within the austenite. Graphite nodules, which have a key role in the growth kinetics of the transformation [6], are not explicitly considered as a micro-constituent in the mentioned models. Finally, Boccardo et al. [7] developed a model taking into account the displacive growth mechanism, in which some microstructure features have been considered such as graphite nodule size, ferrite subunit size, morphology and distribution of phases, and inhomogeneous austenite carbon content. These models are based on representative volume elements (RVE) with large simplifications in the microstructure geometry and carbon diffusion.

In order to carry out a precise prediction of phase evolution during the ausferritic transformation, geometrical features related to graphite nodules (volume fraction, size, and distribution within the matrix) and matrix (size and shape of growing phase) need to be considered. Regarding the carbon distribution in the austenite, it also has to be considered, because the maximum free energy available for nucleation depends on the austenite carbon concentration [8]. One way to model the geometrical details is by means of discrete numerical methods, such as cellular automaton (CA)

CONTACT A. D. Boccardo ✉ aboccardo@frc.utn.edu.ar Instituto de Estudios Avanzados en Ingeniería y Tecnología, IDIT, CONICET-Universidad Nacional de Córdoba, Velez Sarsfield 1611, Córdoba X5000, Argentina

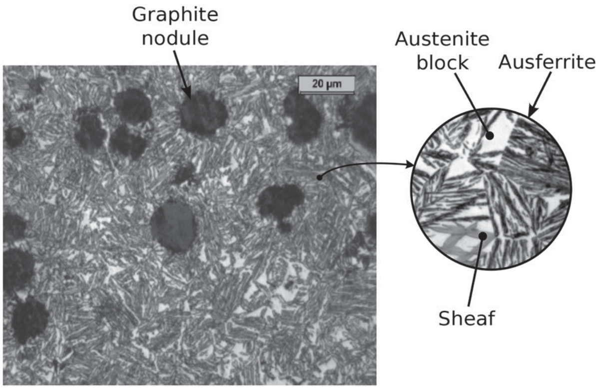

Figure 1. Micrography of an austempered ductile iron.

[9]. In the CA method, the space, time, and state of the physical system are discretized [10]. Each cell has a finite number of states that could change over time according to transition rules. These rules have a key role in the final microstructure and are based on the state of neighbouring cells and the cell itself [11]. The initial morphology and properties of phases are normally introduced in the CA through the digital material representation (DMR) method [12]. The CA method has been applied in the simulation of many microstructural evolution, such as reaustenitization [13], austenite to ferrite transformation [14], dendrites growth [15], recrystallization [16], and ductile iron solidification [17,18], among others.

This paper is concerned with the study of the different phenomena involved at microscale that define the phase evolution during the ausferritic transformation of a ductile iron. The investigation is conducted numerically using a cellular automaton-finite difference analysis (CA-FD). A novel coupled CA-FD model is presented, whose main differences with the previously described models are a detailed description of the ductile iron microstructure and the modelling of carbon diffusion in austenite. In Section 2, the coupled CA-FD model is described. In Section 3, results about the microstructure evolution and carbon distribution during the transformation are discussed. Moreover, the influence of parameters, such as distribution and size of graphite nodules and temperatures, is analysed. Finally, the main conclusions of this work are presented in Section 4.

2. CA-FD model

In this section, a CA-FD model to simulate the ausferritic transformation in ductile iron is described. The model takes into account the size and distribution of graphite nodules, size of ferrite platelets, interaction between growing sheaves, and carbon distribution. CA deals with the microstructure evolution according to the displacive growth mechanism and the FD solves the carbon diffusion.

2.1. Initial microstructure

The initial ductile iron microstructure is formed by graphite nodules embedded in an austenitic matrix. The required micro-constituent features are introduced in the model through the DMR method.

For this analysis, a cubic shape domain (Ω_{cube}) with a periodic geometry is proposed, in which the graphite nodules are modelled as spheres. The nodules are grouped in sets according to their sizes. Each set is characterised by both nodule radius and nodule numbers. The dimension of the cubic domain is appropriated to include the nodule sets and to satisfy a required volume fraction of graphite nodules that ranges between $0.05 \leq f_{Gr} \leq 0.15$ (dilute case). A random, statistically homogeneous, and isotropic spatial distribution of nodules in the domain is performed by the random sequential addition process [19]. The centre coordinates of non-overlapping nodules are obtained with a uniform pseudo-random number generator. The volume fraction of graphite nodules can be obtained from experimental tests or from models that take into account the mass conservation of alloy elements.

Regarding the micro-constituent chemical composition, the graphite nodule carbon concentration is set, in weight per cent (wt-%), as $c_{Gr} = 100$ because it is formed by carbon [7]. The austenite chemical composition is proposed as uniform in the domain and equal to the nominal chemical composition of the ductile iron, except for the carbon content that depends on the temperature at which the ductile iron is austenitized, which is calculated in wt-% with the following expression [2]:

$$\begin{aligned} c_{\gamma_o} &= 0.335 \times 10^{-3}(T_\gamma - 273) \\ &\quad + 1.61 \times 10^{-6}(T_\gamma - 273)^2 + 0.006\mathrm{Mn}{-}0.11\mathrm{Si} \\ &\quad - 0.07\mathrm{Ni} + 0.014\mathrm{Cu}{-}0.3\mathrm{Mo}{-}0.435 \end{aligned} \tag{1}$$

where Mn, Si, Ni, Cu, and Mo are the contents of alloy elements in the ductile iron in wt-%, and T_γ is the austenitizing temperature in K.

2.2. Phase evolution

According to the displacive growth mechanism, ferrite platelets are formed when the thermodynamic criteria for both nucleation (Equation (2)) and growth (Equation (3)) are satisfied [8]:

$$\Delta Gm < Gn \tag{2}$$

$$\Delta G^{\gamma \rightarrow \alpha} < G_{sd} \tag{3}$$

where ΔGm is the maximum free energy available for paraequilibrium nucleation, Gn is the minimum energy necessary to obtain a detectable amount of ferrite, $\Delta G^{\gamma \rightarrow \alpha}$ is the free energy change for the transformation of austenite into ferrite, and G_{sd} is the stored energy due to the shape deformation. The carbon enrichment of austenite modifies the magnitude of ΔGm and $\Delta G^{\gamma\rightarrow\alpha}$. If the austenite carbon concentration is high enough, either one or both thermodynamic criteria are not satisfied and the ausferritic transformation stops. In the ausferritic transformation, $c_{\gamma_{T_{0'}}}$ is the maximum carbon concentration that can be reached in the austenite.

The phase evolution is simulated by a proposed CA model, in which the 3D domain is uniformly divided in an orthogonal arrangement of cubic cells with size cd [20]. During the ausferritic transformation, the temperature is assumed to be uniform in the entire domain and equal to the austempering temperature T_A. The micro-constituents considered by the CA model are graphite nodules, austenite blocks, and sheaves. Sheaves are modelled instead of ferrite platelets and austenite films, because ferrite platelet and austenite film are very small and a large number of cells will be necessary to describe their geometry in the whole cubic domain.

A sheaf is a micro-constituent formed by a fixed relation of ferrite platelets and austenite films. In this work, a sheaf is modelled as an octagonal bipyramid (two regular octagonal pyramids with their bases stuck together), whose volume contains ferrite platelets and austenite films, as is schematically represented in Figure 2(a). In the proposed geometry, the pyramid height is $l_{sh} = n_h l_{\alpha p}$, where n_h is the maximum number of ferrite platelets in the height direction (equal to 3 in the representation) and $l_{\alpha p}$ is the length of a ferrite platelet. The circumradius of the pyramid base is $r_{sh} = n_r(t_{\alpha p} + t_{\gamma f})$, where n_r is the number of ferrite platelets in the base in the radial direction (around 5 in the presentation), and $t_{\alpha p}$ and $t_{\gamma f}$ are the thicknesses of a ferrite platelet and an austenite film, respectively.

Each bipyramid is orientated with respect to the domain coordinate system xyz, as is shown in Figure 2(b). The orientation angles θ and φ are calculated as follows:

$$\theta = \theta_{\vec{n}_{Gr}} + 0.2\pi(rv - 0.5) \tag{4}$$

$$\varphi = \varphi_{\vec{n}_{Gr}} + 0.2\pi(rv - 0.5) \tag{5}$$

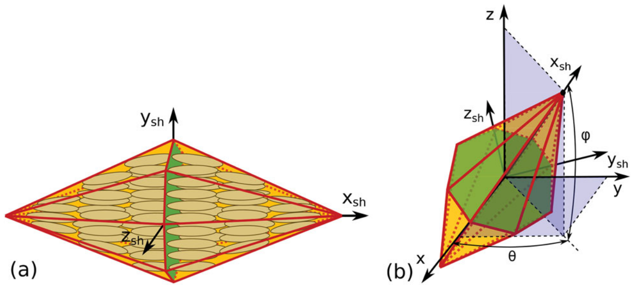

Figure 2. (a) Octagonal bipyramidal representation of a sheaf. (b) Bipyramid orientation with respect to the domain coordinate system *xyz*.

where $\theta_{\vec{n}_{Gr}}$ and $\varphi_{\vec{n}_{Gr}}$ are the angles of the normal vector to the nodule surface, with respect to xyz coordinate system, and rv is a random variable that varies in the range of $0 \leq rv \leq 1$ with a uniform distribution.

The normal vector to the nodule surface, represented in Figure 3, is calculated as follows:

$$\vec{n}_{Gr} = -\sum_{i=1}^{k} \vec{c}_{Gr_i} \tag{6}$$

where k is the number of graphite cells in the Moore neighbourhood of a nodule/austenite interface cell, which is an austenite cell placed next to a graphite nodule cell, and $\vec{c}_{Gr} = (x_{Gr} - x_{ic})\hat{i} + (y_{Gr} - y_{ic})\hat{j} + (z_{Gr} - z_{ic})\hat{k}$ is the position vector of a graphite cell with respect to the nodule/austenite interface cell. x_{Gr}, y_{Gr}, and z_{Gr} are the coordinates of the graphite cell, and x_{ic}, y_{ic}, and z_{ic} are the coordinates of the nodule/austenite interface cell.

At the beginning of the simulation, each austenite cell is set with an uncaptured state (cell without a nucleus of a sheaf). The phase transformation starts with the nucleation of sheaves at nodule/austenite interface cells. When an austenite cell is nucleated, its state is changed to captured. When the bipyramid starts to grow, the cell is set as a sheaf. The procedure employed for the nucleation of each sheaf is schematically illustrated in the flow diagram of Figure 4, in which the questions are Q1: Is the austenite cell in an uncaptured state? and Q2: Is the carbon concentration of the austenite cell lesser than $c_{\gamma_{T_{0'}}}$?.

Based on the work of Ref. [7], a continuous nucleation rate law is proposed:

$$\dot{N}_{nai} = \frac{N_{nai}^{\max}}{t_{inc}} \tag{7}$$

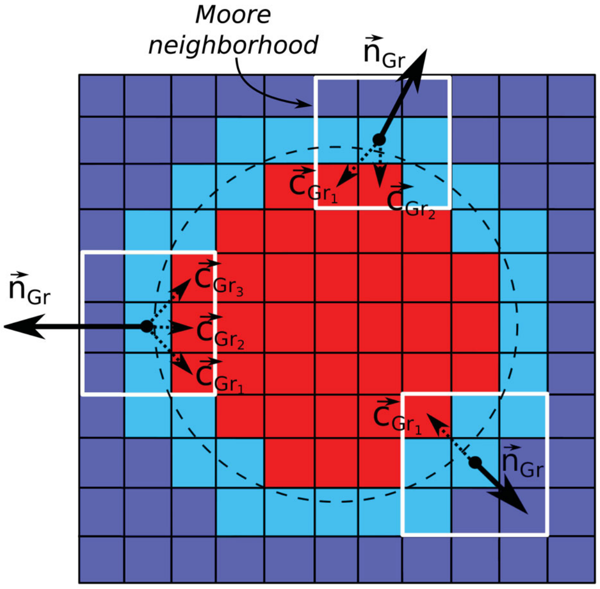

Figure 3. Vector normal to the nodule surface (2D representation). Nodule cells are shown in red, nodule/austenite interface cells in cyan, and austenite block cells in blue. (Colour online)

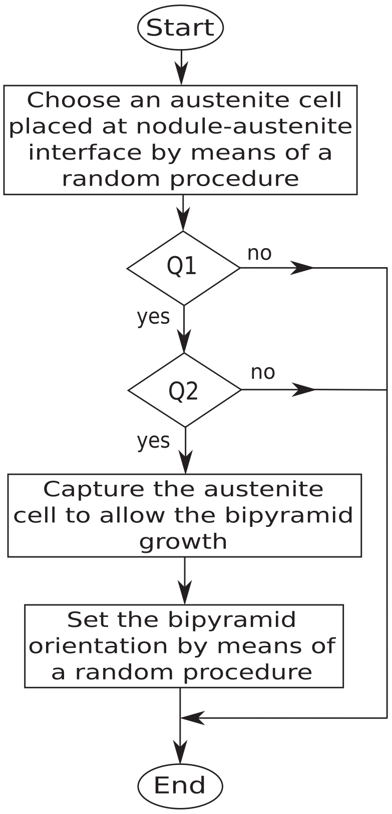

Figure 4. Flow diagram of the nucleation of a sheaf at a nodule/austenite interface cell.

where $\dot{N}_{nai}$ is the number of nodule/austenite interface cells, per unit of time, in which sheaves are nucleated, $N_{nai}^{\max}$ is the maximum number of interface cells in which sheaves are nucleated, and t_{inc} is the incubation time of a ferrite subunit.

The maximum number of interface cells in which sheaves are nucleated is calculated as $N_{nai}^{\max} = (f_{\alpha p}^{\max} l_{\alpha p} s_{Gr})/u_{\alpha p}$, where $f_{\alpha p}^{\max}$ is the maximum volume fraction of ferrite platelets that can be formed around the nodules when the transformation time is equal to t_{inc}, s_{Gr} is the total surface of graphite nodules, and $u_{\alpha p}$ is the volume of a ferrite platelet. The numerator $(f_{\alpha p}^{\max} l_{\alpha p} s_{Gr})$ represents the volume of ferrite platelets that is formed around the nodules at time t_{inc}. The maximum volume fraction of ferrite platelets is computed with Equation (8) [21]. The length, in m, and volume, in m^3, of a ferrite platelet are computed with Equations (9) and (10) [22], respectively.

$$f_{\alpha p}^{\max} = \frac{c_{\gamma_{To'}} - c_{\gamma_o}}{c_{\gamma_{To'}} - c_{\alpha p}} \tag{8}$$

$$l_{\alpha p} = 1 \times 10^{-5}(T_A - 528)/150 \tag{9}$$

$$u_{\alpha p} = 2 \times 10^{-17}[(T_A - 528)/150]^3 \tag{10}$$

where $c_{\alpha p}$ is the ferrite platelet carbon concentration that is set, in wt-%, as $c_{\alpha p} = 0.03$ [21]. The value of $c_{\gamma_{To'}}$ is calculated, in wt-%, as follows [2]:

$$\begin{aligned} c_{\gamma_{To'}} &= 3.072 - 0.0016(T_A - 273) - 0.24\mathrm{Si} \\ &\quad - 0.161\mathrm{Mn} - 0.115\mathrm{Ni} + 0.25\mathrm{Cu} \\ &\quad + 0.06\mathrm{Mo} + 2.69\mathrm{Cr} \end{aligned} \tag{11}$$

where Mn, Si, Ni, Cu, Mo, and Cr are the contents of alloy elements in the ductile iron in wt-%, and T_A is the austempering temperature in K.

The incubation time of a ferrite subunit, in s, is calculated with the expression proposed by Matsuda and Bhadeshia [22]

$$t_{inc} = \frac{k_1}{\nu} \exp\left[\frac{k_2}{RT_A}\left(1 + \frac{\Delta Gm}{k_3}\right)\right] \tag{12}$$

where ν is the attempt frequency factor defined as $\nu = k_b T_A/h$, with k_b and h being the Boltzmann and Planck constants, respectively, R is the universal gas constant, and k_1, k_2, and k_3 are constants. k_1 and k_2 are constants to be fitted and $k_3 = 2540$ J/mol. The maximum free energy available for paraequilibrium nucleation is calculated, taking into account the austenite carbon content of each cell, as in Ref. [7]:

$$\Delta Gm = \Delta Gm_o - f_{ab}(\Delta Gm_o - Gn) \tag{13}$$

where ΔGm_o is the maximum free energy available for paraequilibrium nucleation when the transformation begins and it is evaluated using the parallel tangent construction described in Ref. [23]. The minimum energy Gn is calculated as in Ref. [22]. Finally, f_{ab} is a function that allows ΔGm to take into account the austenite carbon concentration and it is calculated for each cell as $f_{ab} = (c_{\gamma^{cap}} - c_{\gamma_o})/(c_{\gamma_{To'}} - c_{\gamma_o})$, where $c_{\gamma^{cap}}$ is the austenite carbon concentration of the cell when it was captured.

The sheaf growth occurs by the formation of ferrite platelets, which involves autocatalytic nucleation and growth processes. Taking into account that a ferrite platelet grows very fast [22], the growth rate of the length (pyramid height) and radius (pyramid circumradius) of a sheaf are calculated as follows:

$$\dot{l}_{sh} = \frac{l_{\alpha p}}{t_{inc}} \tag{14}$$

$$\dot{r}_{sh} = \frac{t_{\alpha p} + t_{\gamma f}}{t_{inc}} \tag{15}$$

Taking into account that the relation between the volume fractions of austenite films and ferrite platelets in a sheaf is $f_{\gamma f}/f_{\alpha p} = 0.12$ [7], the thickness of an austenite film is assumed as $t_{\gamma f} = 0.12 t_{\alpha p}$. According to the geometrical description of a ferrite subunit presented in Ref. [22], the thickness of a ferrite platelet is assumed as $t_{\alpha p} = l_{\alpha p}/10$.

To allow the sheaf growth within the domain, the austenite cells are captured by employing an algorithm based on the decentered square algorithm proposed for dendrites growth [24]. The sheaf starts growing in the centre of a nucleated cell with a certain orientation. When a corner of the octagonal bipyramid touches an austenite cell places in the Moore neighbourhood, this austenite cell is captured and a new octagonal bipyramid starts growing within it. The bipyramid in the captured cell has the same orientation as that of the bipyramid of the captor cell, but the growth rate is according to its carbon content. The procedure employed for the capture of each austenite cell is schematically illustrated in the flow diagram of Figure 5, in which the questions are Q1: Is the austenite cell in an uncaptured state?; Q2: Is the carbon concentration of the austenite cell lesser than $c_{\gamma_{To'}}$?; and Q3: Is the austenite cell touched for some bipyramid that is growing in a sheaf cell placed at the Moore neighbourhood?. Moreover, the capture process is illustrated in Figure 6 for different transformation times for a 2D case.

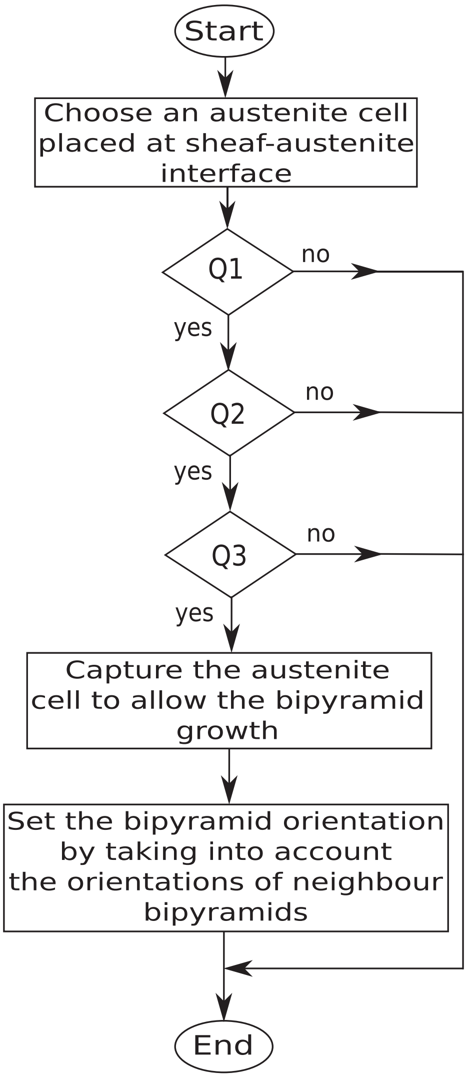

Figure 5. Flow diagram of the capture process of an austenite cell placed at the sheaf/austenite interface.

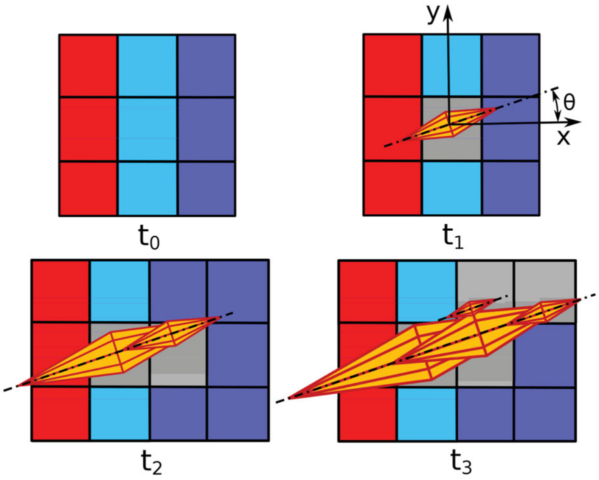

Figure 6. 2D representation of the capture process in the sheaf growth. Nodule cells are shown in red, nodule/austenite interface cells in cyan, austenite block cells in blue, and sheaf cells in grey. (Colour online)

The volume fractions of graphite nodules (f_{Gr}), sheaves (f_{sh}), and austenite blocks ($f_{\gamma b}$) are calculated as follows:

$$f_i = \frac{nc_i}{nc} \tag{16}$$

where nc_i is the number of cells with state i and nc is the total number of cells. The subscript i stands for graphite nodules, sheaves, and austenite blocks.

Taking into account that the volume fraction of austenite films in sheaves is $f_{\gamma f} = 0.12 f_{\alpha p}$ [7], the volume fractions of ferrite platelets and austenite films are computed with the next equations:

$$f_{\alpha p} = 0.89286 f_{sh} \tag{17}$$

$$f_{\gamma f} = 0.10714 f_{sh} \tag{18}$$

Finally, the austenite volume fraction (total) is computed as follows:

$$f_{\gamma} = f_{\gamma f} + f_{\gamma b} \tag{19}$$

2.3. Carbon distribution

After the growth of a carbon-supersaturated ferrite platelet within a sheaf, its excess carbon content is rejected. It is proposed that part of this carbon is incorporated in the austenite films, which are placed within the sheaf, and the other is rejected to the austenite block (placed outside the sheaf). It is considered that the excess of carbon content in ferrite is instantaneously rejected because the coefficient of carbon diffusion in the ferrite is high [25,26]. Additionally, the austenite carbon content in austenite films is $c_{\gamma_{To'}}$, which is immediately reached because films are small and placed next to the ferrite platelets [27]. The increment of carbon concentration, in wt-%, that receives a cell of austenite

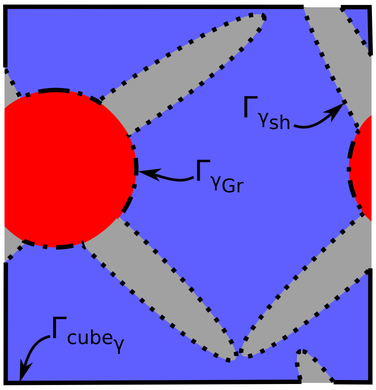

Figure 7. Austenite boundaries at which boundary conditions are applied. Nodule is shown in red, austenite block in blue, and sheaf in grey. (Colour online)

block from sheaf cells is calculated as follows:

$$\Delta c_\gamma = \sum_{i=1}^{k}\left[\Delta fn_{sh_i}\frac{(c_{\gamma_i^{cap}} - c_{sh})}{nc_{\gamma_i}}\right] \tag{20}$$

where $\Delta fn_{sh} = \Delta v_{sh}/v_{cell}$, Δv_{sh} is the increment of sheaf volume in a sheaf cell, v_{cell} is the cell volume, c_{sh} is the sheaf carbon concentration, nc_{γ_i} is the number of austenite cells that are able to receive carbon from the sheaf cell ($c_\gamma < c_{\gamma_{To'}}$), and k is the number of sheaf cells placed in the Moore neighbourhood of the austenite cell. Taking into account that the volume fraction of austenite films in a sheaf is $f_{\gamma f} = 0.12 f_{\alpha p}$ [7], the sheaf carbon concentration is calculated as $c_{sh} = 0.89286 c_{\alpha p} + 0.10714 c_{\gamma_{To'}}$.

The carbon diffusion within the austenite block domain (Ω_γ) is calculated based on the diffusion equation:

$$\frac{\partial c_\gamma}{\partial t} = \mathrm{div}(\mathbf{D}_\gamma \,\mathrm{grad}(c_\gamma)) \tag{21}$$

where $\mathbf{D}_\gamma$ is the isotropic carbon diffusion tensor of second-rank defined as $\mathbf{D}_\gamma = D_\gamma \mathbf{1}$, where D_γ is the coefficient of carbon diffusion in austenite and $\mathbf{1}$ is the unit tensor of second-rank.

Equation (21) is valid in $\Omega_\gamma \times \Upsilon$, where Υ denotes the time interval of interest with time $t \in \Upsilon$. This equation is solved by the implicit finite difference method using a grid with the same size that the employed for the CA model. The considered boundary conditions are: (a) periodic boundary condition at a cube boundary formed by austenite (Γ_{cube_γ}) and (b) Neumanm boundary condition (normal carbon flux equal to zero) at austenite–graphite ($\Gamma_{\gamma_{Gr}}$) and austenite–sheaf ($\Gamma_{\gamma_{sh}}$) boundaries, see Figure 7.

The coefficient of carbon diffusion in austenite depends on both austempering temperature and austenite carbon concentration, and it is calculated, in m^2/s, with the following equation [28]:

$$\begin{aligned} D_\gamma = 4.53 \times 10^{-7}\left[1 + y_c(1-y_c)\frac{8339.9}{T_A}\right] \\ \times \exp\left\{-\left[\frac{1}{T_A} - 2.221 \times 10^{-4}\right]\right. \\ \left.\times\ (17767 - 26436 y_c)\right\} \end{aligned} \tag{22}$$

where $y_c = x_c/(1 - x_c)$, with x_c being the ordinary mole fraction of carbon in austenite.

2.4. Retained austenite at ambient temperature

When the material is cooled down from austempering temperature to ambient temperature and the austempering time is not large enough, the austenite is able to transform into martensite. In order to predict the amount of retained austenite at ambient temperature for different austempering times, the following model is proposed. It is assumed that only austenite block cells are able to transform into martensite because the carbon concentration of austenite films is large enough to get $T_{MS} < T_{amb}$, where T_{MS} is the martensite start temperature and T_{amb} is the ambient temperature. The martensite volume fraction formed in each austenite block cell ($f_{m_{cell}}$), with respect to the cell volume fraction, is computed with the expression proposed by Khan and Bhadeshia [29]:

$$f_{m_{cell}} = 1 - \exp\{-f_{m_{cell}}[1 + k_4(T_{MS} - T_{amb})]\} \tag{23}$$

where k_4 is a constant to be fitted.

For each austenite block cell the temperature T_{MS} is computed, in K, with the following equation from Ref. [30]:

$$\begin{aligned} T_{MS} = 772 - 300C_\gamma - 33.3\mathrm{Mn} - 11.1\mathrm{Si} - 22.2\mathrm{Cr} \\ - 16.7\mathrm{Ni} - 11.1\mathrm{Mo} \end{aligned} \tag{24}$$

where C_γ is the content of carbon in austenite and Mn, Si, Cr, Ni, and Mo are the contents of alloy elements in the ductile iron, all in wt-%.

The volume fractions of martensite (f_m) and retained austenite ($f_{\gamma ret}$) are computed as follows:

$$f_m = \sum_{i=1}^{n\gamma b}\frac{f_{m_{cell_i}}}{nc} \tag{25}$$

$$f_{\gamma ret} = 1 - (f_{Gr} + f_{sh} + f_m) \tag{26}$$

where $n\gamma b$ is the number of austenite block cells.

2.5. Numerical implementation

This model was computationally implemented using Fortran language (non-parallelized code) and the visualisation was performed with the Paraview software. A flow diagram of the model is schematically shown in Figure 8. The required input data are chemical composition of ductile iron, austenitization and austempering temperatures, austempering time (t_s), set numbers of graphite nodules, size and number of graphite nodules per set, graphite volume fraction, constants k_1, k_2, and k_4, time step (Δt), and cell dimension.

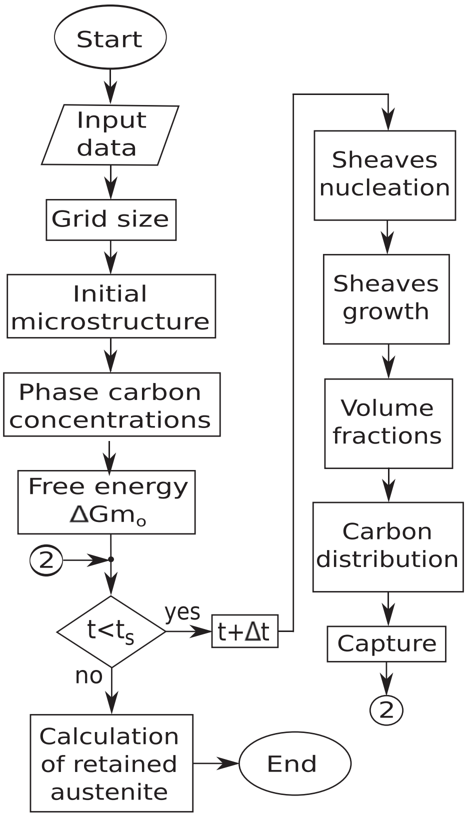

Figure 8. Flow diagram of the proposed CA-FD model.

3. Results and discussion

3.1. Development of phase transformation

In order to investigate how the ausferritic transformation is developed, the simulation for a cubic domain with one graphite nodule of radius 6×10^{-6} m is performed. The following input data are considered: graphite volume fraction $f_{Gr} = 0.1$, chemical composition 3.70 C–2.7 Si–0.1 Mn–0.02 P–0.01 S–0.04Mg (in wt-%), and temperatures $T_\gamma = 1173$ K (900°C) and $T_A = 673$ K (400°C). The incubation time constants $k_1 = 1.8016 \times 10^{15}$ and $k_2 = 158.79$ J/mol were obtained by fitting the model response to the experimental data presented in Ref. [6] employing the procedure explained in Ref. [7]. The cell dimension ($cd = 5.5 \times 10^{-7}$ m) and time step ($\Delta t = 5$ s) were determined by means of a convergence study.

Figure 9(a) shows the graphite, austenite (total), and ferrite platelet volume fractions during the ausferritic transformation. The ferrite platelet volume fraction has a sigmoidal behaviour, starting from zero up to its maximum volume fraction. The austenite volume fraction has the opposite behaviour because it is consumed by the ferrite platelets. Finally, the graphite volume fraction remains constant during all the transformation.

The transformation development is divided into stage 1, growth without micro-constituent contact, and stage 2, growth with contact. In stage 1, the nucleation of sheaves starts at the nodule/austenite interface. This nucleation process increases the number of sheaves and it has a remarkable influence on the development of the ausferritic transformation up to $t \approx 200$ s. After a sheaf is nucleated, the growth process is developed at the sheaf/austenite interface. The sheaf

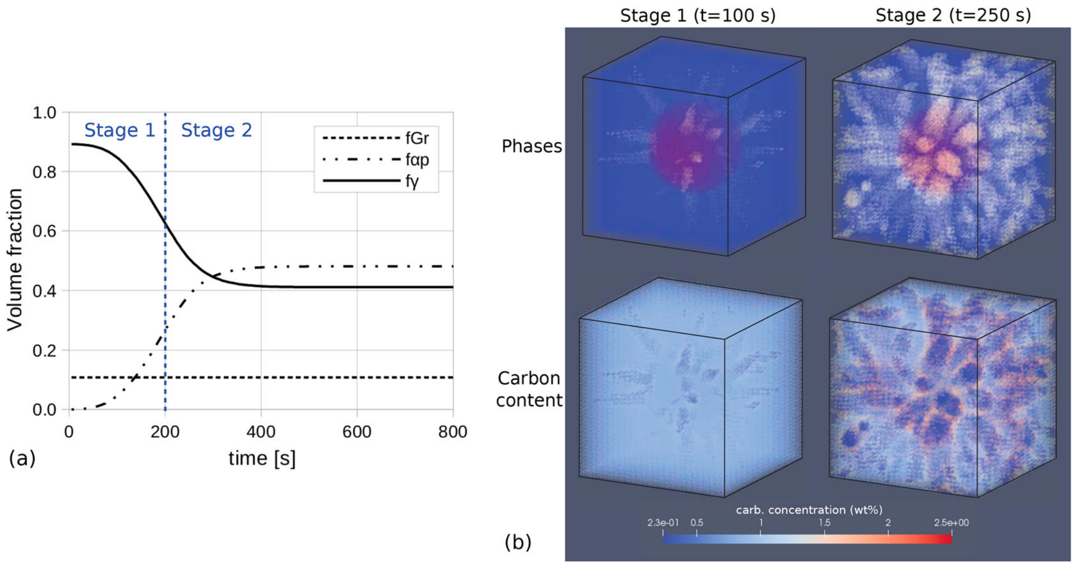

Figure 9. (a) Evolution of phase fractions during ausferritic transformation. (b) Phases and carbon content in the domain at 100s and 250s. Graphite nodule is shown in red, sheaves in white, and austenite block in blue. The nodule is not included in the carbon content visualisation. (Colour online)

orientations are close to the normal to the nodule surface. During stage 1, the sheaf/austenite interface surface is increased and it contributes to the increment of the growth rate, because more surface is available for autocatalytic nucleation. Stage 2 starts when the lengths of sheaves are high enough for them begin to be in contact. At the beginning of this stage, there are few sheaves in contact, and the number of contacts increases as the volume fraction of sheaves increases. The contact between sheaves reduces the sheaf/austenite interface surface, a fact that contributes to the growth rate reduction. Regarding the carbon distribution, a uniform carbon concentration is observed at sheaves during all the transformation. On the other hand, the carbon rejected from sheaves to austenite block is piled up near to the sheaf/austenite interface and the carbon concentration in the austenite placed far from this interface remains close to its initial value. This behaviour in the austenite block carbon concentration occurs due to a low coefficient of carbon diffusion in austenite. The carbon concentration at the sheaf/austenite interface is gradually increased during the transformation and it contributes to the reduction of the growth rate due to the increment of the incubation time. When the transformation ends, the austenite carbon concentration becomes uniform and around $c_{\gamma_{To'}}$. Figure 9(b) shows the phases and carbon content in the domain for $t = 100$ s (stage 1) and $t = 250$ s (stage 2).

3.2. Contact between sheaves

The contact between sheaves takes a key role in the growth kinetics of the ausferritic transformation because it contributes to the reduction of the growth rate, as is mentioned in Section 3.1. The contact is established at a certain volume fraction of sheaves, which varies with factors such as the distance between neighbour nodules, the position of sheaves in the nodule surface, and the orientation of sheaves. These factors are random variables and their influences are analysed as follows. Cubic domains with different numbers of nodules of equal size are proposed. A domain that contains one graphite nodule has a rectangular graphite nodule distribution; therefore, the distance between nodules is not a random variable. On the other hand, domains with a number of nodules greater than or equal to two have a random distribution of nodules and different distances between them could exist.

For each domain with a specific number of nodules, a set of multiple realisations (or ensemble of realisations) is obtained with the model. A realisation is referred to as an individual sample characterised by a particular distance between neighbour nodules, position of sheaves in the nodule surface, and orientation of sheaves. In order to alleviate the effects of randomness in realisations and obtain a statistically representative growth kinetics of ferrite platelets, the ensemble averaging procedure is employed [31]. For each transformation time, the average volume fraction is calculated with the following equation:

$$\langle\!\langle f_{\alpha p} \rangle\!\rangle = \frac{1}{m} \sum_{k=1}^{m} f_{\alpha p_k} \tag{27}$$

where m is the number of realisations. A finite number of realisations, to obtain the representative growth kinetics, is found by means of a convergence study. The average fraction is calculated for an increasing number of realisations until the following criterion is satisfied:

$$E_{ea}^{(k+1)} = \left| \frac{\langle\!\langle f_{\alpha p} \rangle\!\rangle^{(k+1)} - \langle\!\langle f_{\alpha p} \rangle\!\rangle^{(k)}}{\langle\!\langle f_{\alpha p} \rangle\!\rangle^{(k)}} \right| < tol_{ea} \tag{28}$$

where tol_{ea} is the convergence tolerance for the ensemble averaging and it is proposed as $tol_{ea} = 0.8\%$. The volume fraction of ferrite platelets at convergence is denoted as $\langle\!\langle f_{\alpha p} \rangle\!\rangle^{(\tilde{\infty})}$.

The representative growth kinetics of ferrite platelets were determined for domains with 1 nodule and 6 nodules employing 22 and 14 realisations, respectively, and are presented in Figure 10(a) in continuous and dashed lines. The upper and lower bounds of these cases are also included in the figure by thin-dashed lines. The evolution of E_{ea} resulting from the convergence study is shown in Figure 10(b). The minimum distance between nodules for the domain with one nodule is around 8.5×10^{-6} m and the average minimum distance between nodules for the domain with six nodules ranges between 1×10^{-6} and 4×10^{-6} m. When the minimum distance between nodules is decreased, the growth rate is reduced because early contact between sheaves occurs. This explains why the representative growth kinetics, during stage 2, is highly influenced by the number of nodules within the domain.

According to the previous finding, a domain with an appropriated number of nodules should be found to obtain a representative growth kinetics taking into account the influence of random distances between neighbour nodules. The representative growth kinetics is found by combining the procedures of ensemble averaging and sample enlargement [31]. In the resulting procedure, the number of nodules within the domains is increased until the following criterion is satisfied:

$${}^{(j+1)}E_{se} = \left| \frac{{}^{(j+1)}\langle\!\langle f_{\alpha p} \rangle\!\rangle^{(\tilde{\infty})} - {}^{(j)}\langle\!\langle f_{\alpha p} \rangle\!\rangle^{(\tilde{\infty})}}{{}^{(j)}\langle\!\langle f_{\alpha p} \rangle\!\rangle^{(\tilde{\infty})}} \right| < tol_{se} \tag{29}$$

where tol_{se} is the convergence tolerance for the sample enlargement and it is proposed as $tol_{se} = 1.74\%$. The volume fraction of ferrite platelets at convergence is denoted as ${}^{(\tilde{\infty})}\langle\!\langle f_{\alpha p} \rangle\!\rangle^{(\tilde{\infty})}$.

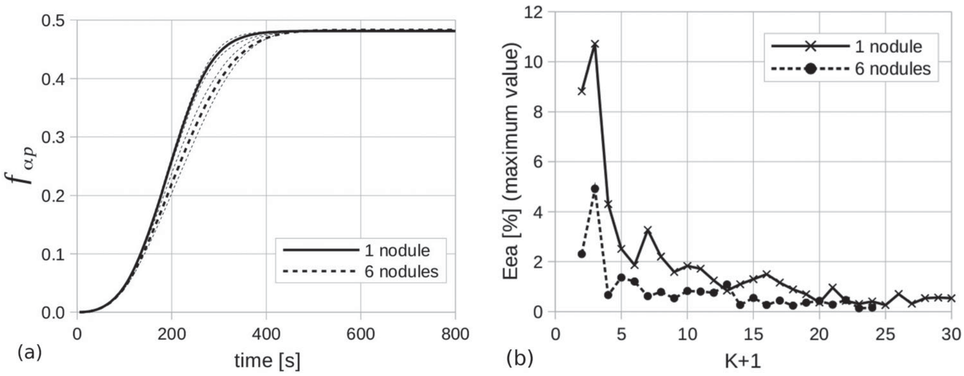

Figure 10. (a) Evolution of ferrite platelet volume fraction during the transformation for domains with one and six nodules. (b) Variation of E_{ea} related to the number of realisations for domains with one and six nodules.

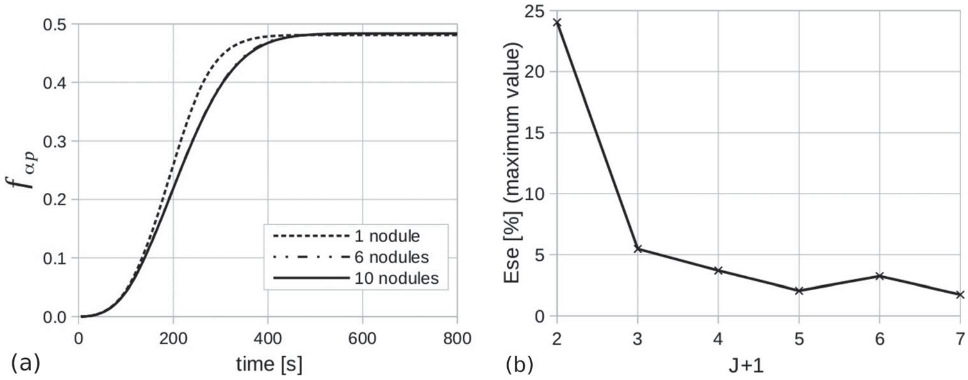

Figure 11. (a) Evolution of ferrite platelet volume fraction during the transformation for domains with 1, 6, and 10 nodules. (b) Variation of E_{se} related to the number of nodules within the domain.

In Figure 11(a), the representative growth kinetics of domains with 1, 6, and 10 nodules are compared. It is observed that the results obtained for domains with 6 and 10 nodules are very close; therefore, the RVE determined by means of the described numerical procedure (numerical RVE) is obtained by the ensemble averaging of random realisations of a cubic domain with six or more graphite nodules. In Figure 11(b), the evolution of E_{se} is presented, showing that it is reduced when the number of nodules increases.

3.3. Influence of graphite nodule size and temperatures

The influences of graphite nodule size, and austenitizing and austempering temperatures on the growth kinetics and final phase fraction are analysed. In order to do that, the model is employed to simulate the ausferritic transformation varying the nodule radius in the range of 6×10^{-6} m $\leq r_{gr} \leq 22 \times 10^{-6}$ m, and the temperatures in the ranges of 1123 K (850°C)$\leq T_{\gamma} \leq$ 1223; K (950°C) and 623 K (350°C)$\leq T_A \leq$ 723 K (450°C). The numerical RVE is formed by the ensemble averaging of 10 random realisations of a cubic domain with 10 graphite nodules of equal size, see Figure 12(a). The cubic domain is discretized with 80 × 80 × 80 cells and the time step is $\Delta t = 5$ s. The number of cells for the spatial discretization and the time step for the time discretization were obtained by means of a convergence study. The required time to solve each realisation is about 2 hours on a desktop PC with an i7 Intel microprocessor of the fifth generation. This time depends strongly on the spatial discretization.

The growth kinetics of ferrite platelets is modified by the nodule size, and the austenitizing and austempering temperatures, as is shown in Figure 12(b). In different processes such as heat treatments, it is important to determine the required time to end the ausferritic transformation (t_{RT}); therefore, it is analysed as follows. The t_{RT} is highly influenced by the nodule size and austempering temperature, as is observed in Figure 13(a). When the nodule size decreases, the t_{RT} decreases. This behaviour occurs because a nodule size decrement increases the relation nodule surface–total volume ($S_{Gr}/V_t = 3f_{Gr}/r_{gr}$) that allows us to increase the nucleation rate per unit of volume, which increases the growth rate during stage 1 of the transformation. When the austempering temperature decreases, t_{RT} increases, because the dimension of ferrite platelets decreases reducing the growth rate. The austenitization temperature has a minor influence, increasing t_{RT} when the temperature increases. An increment in the austenitizing temperature increases the initial austenite carbon concentration which in turn increases the incubation time. The increment of the incubation time decreases

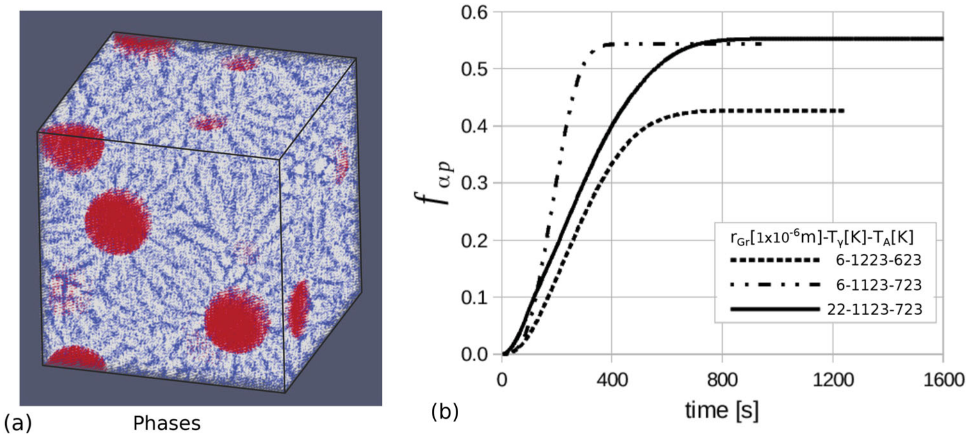

Figure 12. (a) Phases at the end of the ausferritic transformation. Domain with 10 nodules of $r_{gr} = 6 \times 10^{-6}$ m, $T_\gamma =$ 1173 K (900°C), and $T_A =$ 623 K (350°C). Graphite nodules are shown in red, sheaves in white, and austenite block in blue. (b) Evolution of ferrite platelet volume fraction during the ausferritic transformation for different nodule size, and austenitizing and austempering temperatures. (Colour online)

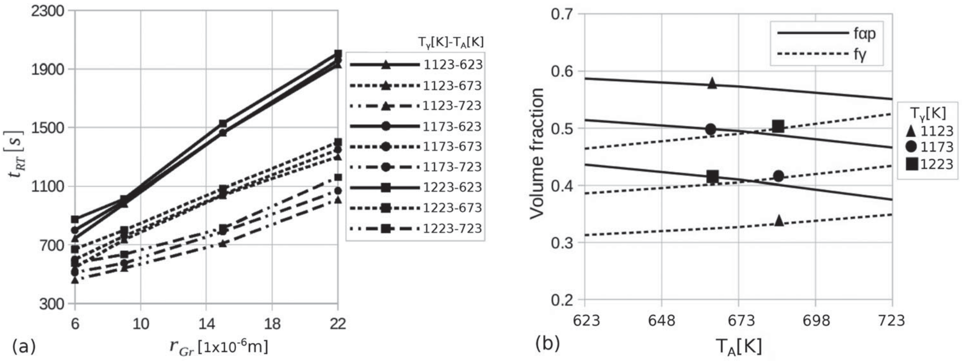

Figure 13. (a) Required time to end the ausferritic transformation for different nodule size, and austenitizing and austempering temperatures. (b) Volume fractions of ferrite platelets and austenite, at the end of the transformation, as a function of austenitizing and austempering temperatures.

the growth rate. The same influence of nodule size and austempering temperature was reported in Ref. [6].

The ferrite platelets and austenite volume fractions, at the end of the ausferritic transformation, depend on the temperatures and their variations are shown in Figure 13(b). The volume fraction of ferrite platelets increases with a decrement of both austenitizing and austempering temperatures. The decrement of austenitizing temperature reduces the initial austenite carbon concentration and a decrement of austempering temperature allows us to increase the austenite carbon concentration at the end of the transformation. Owing to the mentioned variations, the increment of carbon concentration that austenite is able to receive during the transformation increases. A large increment of austenite carbon concentration allows us to extend the transformation of austenite into ferrite platelets, explaining the observed behaviour. On the other hand, the austenite volume fraction has an opposite behaviour to the ferrite platelets one, because the austenite is consumed by the second phase. The same influence of austenitizing and austempering temperatures was reported in Ref. [2].

3.4. *Comparison with experimental data*

The numerical results are compared with experimental data extracted from Refs. [6,32,33], in which ductile irons with different chemical compositions and graphite nodule counts were heat treated at different temperatures as is shown in Table 1.

The numerical RVE is formed by the ensemble averaging of 16 random realisations of a cubic domain with six graphite nodules. The sizes of graphite nodules employed in the simulation are presented in Table 2. For cases Exp1, Exp2, Exp3, and Exp4, two sizes of graphite nodules were considered. The incubation time constants are $k_1 = 1.8016 \times 10^{15}$ and $k_2 = 158.79$ J/mol. The constant $k_4 = 6.6 \times 10^{-3}$ was obtained by fitting the model response to the experimental data presented in Ref. [33]. The cubic domain is discretized with $80 \times 80 \times 80$ cells and the time step is $\Delta t = 5$ s. The number of cells for the spatial discretization and the time step for the time discretization were obtained by means of a convergence study.

Figure 14 compares the evolution of both normalised ferrite platelet volume fraction $f_{\alpha p_n}$ (model result)

Table 1. Characteristics of ductile iron and austempering heat treatment (extracted from experimental tests of Refs. [6,32,33]).

Case	Si	Mn	Cu	Ni	Mo	f_{Gr}	Nodule count [1×10^6 nod/mm^2]	T_γ [K (°C)]	T_A [K (°C)]
Exp1	2.7	0.1	–	–	–	0.1	330	1193(920)	673(400)
Exp2	2.7	0.1	–	–	–	0.1	1992	1193(920)	673(400)
Exp3	2.7	0.1	–	–	–	0.1	1992	1193(920)	623(350)
Exp4	2.7	0.1	–	–	–	0.1	1992	1193(920)	573(300)
Exp5	2.32	0.59	0.29	–	0.33	0.12	230	1143(870)	648(375)
Exp6	2.51	0.56	0.31	–	0.15	0.12	130	1143(870)	648(375)
Exp7	2.64	0.67	0.25	–	0.25	0.12	102	1143(870)	648(375)
Exp8	2.77	0.04	0.33	0.07	–	0.1	180	1173(900)	643(370)
Exp9	2.8	0.02	0.9	1.02	–	0.09	66	1173(900)	643(370)

Table 2. Sizes of graphite nodules employed in the simulation.

Case	Size 1		Size 2	
	r_{gr_1} [1×10^{-6} m]	Number of nodules	r_{gr_2} [1×10^{-6} m]	Number of nodules
Exp1	10	3	12.5	3
Exp2	4	5	7.5	1
Exp3	4	5	7.5	1
Exp4	4	5	7.5	1
Exp5	16.3	6	–	–
Exp6	21.5	6	–	–
Exp7	24.5	6	–	–
Exp8	19	6	–	–
Exp9	30	6	–	–

and normalised dimensional change dc_n (experimental result) during the development of ausferritic transformation, which are normalised with respect to their maximum values. The dimensional change depends on $f_{\alpha p}$ evolution, and it is computed as $dc = \Delta l / l_o$, where l_o is the sample length at the beginning of the ausferritic transformation and $\Delta l = l - l_o$ is the change in the sample length during the transformation. The changes in the evolution with the variations of graphite nodule count, Figure 14(a), and austempering temperature, Figure 14(b), are followed by the proposed CA-FD model. Moreover, a good correlation between numerical and experimental results is observed.

Figure 15 compares the normalised retained austenite volume fractions at ambient temperature $f_{\gamma ret_n}$, for different austempering times, obtained with the model and measured from experiments. The values are normalised with respect to their maximum values. It is observed that the volume fraction of $f_{\gamma ret_n}$ increases with the increment of the austempering time. The amount of retained austenite depends on the development of the ausferritic transformation because austenite receives carbon from ferrite platelets. The temperature

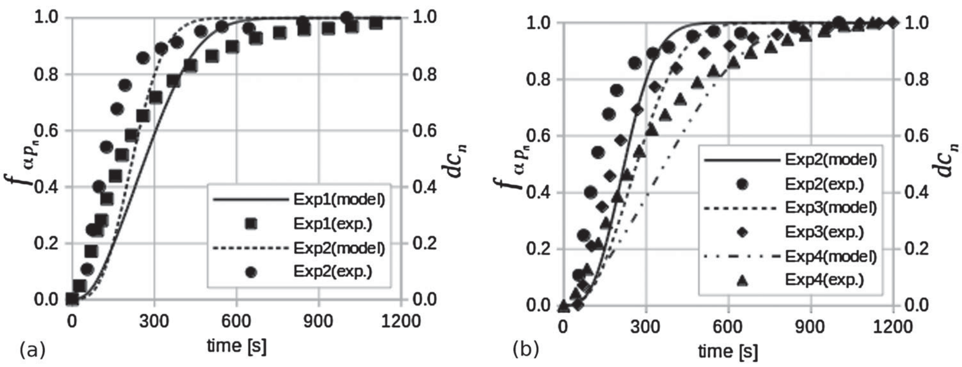

Figure 14. Evolution of normalised ferrite platelet volume fraction and normalised dimensional change for different (a) graphite nodule counts and (b) austempering temperatures.

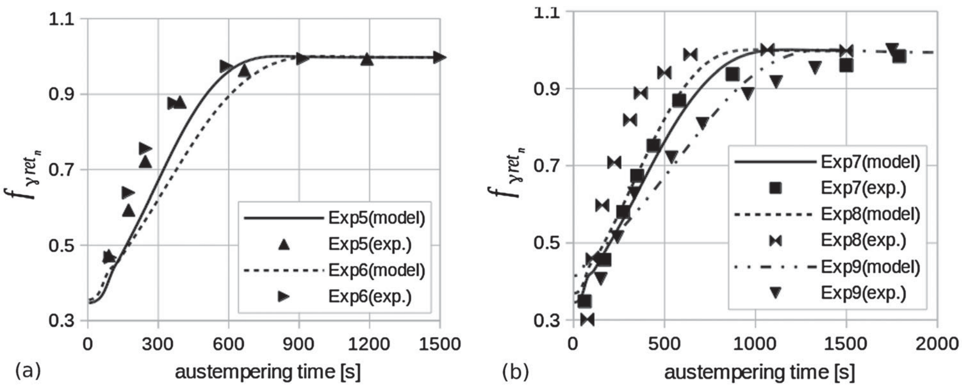

Figure 15. Normalised retained austenite volume fraction for different austempering times.

at which the austenite starts to transform into martensite decreases with an increment of the austenite carbon concentration. The experimental results for different chemical compositions, graphite nodule counts, and heat treatment temperatures are well represented by the proposed CA-FD model.

4. Conclusions

In this paper, a cellular automaton-finite difference model to simulate the ausferritic transformation of ductile iron was presented. The CA model considers the nucleation of sheaves at graphite nodule surfaces. The sheaf growths are computed according to the displacive growth mechanism. The carbon rejected from sheaves is distributed in the austenite by solving the diffusion equation with FD method. The development of the transformation was investigated and the results were compared with experimental data. The main conclusions of this work may be summarised as follows.

1. Two stages could be identified during the development of ausferritic transformation. Stage 1 is characterised by a rising growth rate due to sheaf growths without contact each other. On the other hand, stage 2 is characterised by a decreasing growth rate as a result of contact between sheaves and high austenite carbon content at the sheaf/austenite interface.
2. The contact between sheaves reduces the transformation rate during stage 2. For this reason, the moment at which the contact is established has a key role in the growth kinetics. Early contact appears for graphite nodules distributed in a random position; therefore, the transformation rate is slower than for nodules distributed in a rectangular form.
3. The carbon content rejected from sheaves is piled up close to the sheaf/austenite interface due to a low value of the coefficient of carbon diffusion in austenite at the austempering temperature. As a consequence, a large inhomogeneity of carbon concentration exists in austenite blocks, which finally disappears when the transformation ends.
4. The kinetics of the transformation is highly affected by the variation of both graphite nodule size and austempering temperature. By studying the influence of these parameters on the required time to end the ausferritic transformation (t_{RT}), the conclusions are: (a) increment of t_{RT} with a nodule size increment and (b) increment of t_{RT} with an austempering temperature decrement.
5. The phase volume fractions at the end of the transformation depend only on the austenitizing and austempering temperatures, increasing the ferrite platelet volume fraction with a decrement of both austenitizing and austempering temperatures. The austenite volume fraction has an opposite behaviour to the ferrite platelet one.

Future works could deal with graphite particles of different shapes and initial matrix with no homogeneous distribution of alloy elements. The periodic geometry of the cubic domain could be employed to determine effective mechanical and thermal properties by means of micromechanical analysis.

Acknowledgements

During the course of this research, A.D. Boccardo had a postdoctoral scholarship from CONICET. L.A. Godoy is a member of the research staff of CONICET.

Disclosure statement

No potential conflict of interest was reported by the authors.

Funding

This work was supported by a grant from Universidad Tecnológica Nacional (ASUTNCO0004735).

ORCID

A. D. Boccardo http://orcid.org/0000-0003-3299-2510

References

[1] Bhadeshia HKDH. Bainite in steels. 2nd ed. London: IOM Communications; 2001.
[2] Chang LC. An analysis of retained austenite in austempered ductile iron. Mater Trans A. 2003;34(2):211–217.
[3] Thomson RC, James JS, Putman DC. Modelling microstructural evolution and mechanical properties of austempered ductile iron. Mater Sci Technol. 2000;16(11–12):1412–1419.
[4] Kapturkiewicz W, Burbelko AA, Lelito J, et al. Modelling of ausferrite growth in ADI. Int J Cast Met Res. 2003;16(1–3):287–292.
[5] Hepp E, Hurevich V, Schäfer W. Integrated modeling and heat treatment simulation of austempered ductile iron. IOP Conf Ser: Mater Sci Eng. 2012;33(1):012076.
[6] Fraś E, Górny M, Tyrała E, et al. Effect of nodule count on austenitising and austempering kinetics of ductile iron castings and mechanical properties of thin walled iron castings. Mater Sci Technol. 2012;28(12):1391–1396.
[7] Boccardo AD, Dardati PM, Celentano DJ, et al. A microscale model for ausferritic transformation of austempered ductile irons. Mater Trans A. 2017;48(1):524–535.
[8] Rees GI, Bhadeshia HKDH. Bainite transformation kinetics part 1 modified model. Mater Sci Technol. 1992;8(11):985–993.
[9] Li DZ, Xiao NM, Lan YJ, et al. Growth modes of individual ferrite grains in the austenite to ferrite transformation of low carbon steels. Acta Mater. 2007;55(18):6234–6249.
[10] Raghavan S, Sahay SS. Modeling the topological features during grain growth by cellular automaton. Comput Mater Sci. 2009;46(1):92–99.
[11] Halder C, Madej L, Pietrzyk M. Discrete micro-scale cellular automata model for modelling phase transformation during heating of dual phase steels. Arch Civ Mech Eng. 2014;14(1):96–103.

[12] Sieradzki L, Madej L. A perceptive comparison of the cellular automata and Monte Carlo techniques in application to static recrystallization modeling in polycrystalline materials. Comput Mater Sci. 2013;67: 156–173.

[13] Yang BJ, Chuzhoy L, Johnson ML. Modelling of reaustenitization of hypoeutectoid steels with cellular automaton method. Comput Mater Sci. 2007;41(2): 186–194.

[14] Lan YJ, Li DZ, Li YY. Modeling austenite decomposition into ferrite at different cooling rate in low-carbon steel with cellular automaton method. Acta Mater. 2004;52(6):1721–1729.

[15] Beltran-Sanchez L, Stefanescu DM. Growth of solutal dendrites: a cellular automaton model and its quantitative capabilities. Mater Trans A. 2003;34(2): 367–382.

[16] Song KJ, Dong ZB, Fang K, et al. Cellular automaton modelling of dynamic recrystallisation microstructure evolution during friction stir welding of titanium alloy. Mater Sci Technol. 2014;30(6):700–711.

[17] Dardati PM, Godoy LA, Cervetto GA, et al. Simulación de la micromecánica en la solidificación de una fundición de grafito esferoidal [Micromechanics simulation during the solidification of SG cast-iron]. Rev Int Mét Num Cálc Dis Ing. 2005;21(4):327–344. Spanish.

[18] Burbelko AA, Gurgul D, Kapturkiewicz W, et al. Cellular automaton modeling of ductile iron microstructure in the thin wall. Arch Foundry Eng. 2011;11(4): 13–18.

[19] Rintoul MD, Torquato S. Reconstruction of the structure of dispersions. J Colloid Interface Sci. 1997;186(2): 467–476.

[20] Chen R, Xu Q, Liu B. Cellular automaton simulation of three-dimensional dendrite growth in Al-7Si-Mg ternary aluminum alloys. Comput Mater Sci. 2015;105:90–100.

[21] Yescas MA, Bhadeshia HKDH. Model for the maximum fraction of retained austenite in austempered ductile cast iron. Mater Sci Eng A. 2002;333(1–2):60–66.

[22] Matsuda H, Bhadeshia HKDH. Kinetics of the bainite transformation. Proc R Soc Lond A. 2004;460(2046): 1707–1722.

[23] Bhadeshia HKDH. Thermodynamic analysis of isothermal transformation diagrams. Metal Sci. 1982;16(3): 159–166.

[24] Wang W, Lee PD, McLean M. A model of solidification microstructures in nickel-based superalloys: predicting primary dendrite spacing selection. Acta Mater. 2003;51(10):2971–2987.

[25] Mujahid SA, Bhadeshia HKDH. Partitioning of carbon from supersaturated ferrite plates. Acta Metall Mater. 1992;40(2):389–396.

[26] Ławrynowicz Z, Dymski S. Analysis of carbon diffusion during bainite transformation in ADI. Arch Foundry Eng. 2007;7(3):87–92.

[27] Rees GI, Bhadeshia HKDH. Bainite transformation kinetics part 2 non-uniform distribution of carbon. Mater Sci Technol. 1992;8(11):994–1003.

[28] Ågren J. A revised expression for the diffusivity of carbon in binary Fe-C austenite. Scr Mater. 1986;20(11): 1507–1510.

[29] Khan SA, Bhadeshia HKDH. Kinetics of martensite transformation in partially bainitic 300M Steel. Mater Sci Eng A. 1990;129(2):257–272.

[30] Nehrenberg AE. Technical publication 2059: Discussion, Iron and Steel Division. Met Technol (N Y). 1946;XIII:33–43. http://library.aimehq.org/library/metals-technology-1946-vol-xiii.html

[31] Temizer I. Micromechanics: Analysis of heterogeneous materials. Turkey: Department of Mechanical Engineering, Bilkent University. Available from: https://sourceforge.net/projects/multiscale.2012.

[32] Darwish N, Elliott R. Austempering of low manganese ductile irons. Mater Sci Technol. 1993;9(7):572–585.

[33] Liu J, Elliott R. The influence of cast structure on the austempering of ductile iron. Part 3: the role of nodule count on the kinetics, microstructure and mechanical properties of austempered Mn alloyed ductile iron. Int J Cast Met Res. 1999;12(3):189–195.